



Assessment and comparison of tonal noise models for Counter-Rotating Open Rotors

Laurent Soulat*, Irwin Kernemp†, Marlène Sanjose‡, Stéphane Moreau§

Aeroacoustics Group, Université de Sherbrooke, Sherbrooke, QC, Canada

Rasika Fernando¶

Sneecma, Acoustics Department, Moissy-Cramayel, France

A hybrid method combining a three-dimensional unsteady RANS simulation of a cropped CROR at approach conditions and an acoustic analogy either based on a time formulation, an advanced-time formulation of Ffowcs-Williams and Hawkings' analogy, or on a frequency formulation, an extension of Hanson's model to non compact chord length, has shown three main sources, the impacts of the front-rotor wakes on the aft-rotor, of the front-rotor tip vortex on the aft-rotor tip, and of the front-rotor hub horse-shoe vortex on the aft-rotor foot. Consequently, this study confirms that the aft-rotor is the dominant tonal noise source and has identified another potential noise source when the CROR is installed caused by the strong tip vortex of the highly-loaded clipped aft-rotor. The rotor-rotor distance should not be reduced as the potential effect is already felt on the front rotor. The influence of several numerical parameters including grid refinement, data sampling and simulation length has been evaluated on both aerodynamic and acoustic performances.

I. Introduction

Counter-Rotating Open Rotors (CROR) in the low- to medium range transportation are seen as good propulsion systems to significantly improve the specific fuel consumption of the next generations of aircrafts.¹ Nevertheless, the acoustic design is very critical for this kind of configurations,² and has been a major obstacle so far for its installation on aircrafts. Indeed, the aerodynamic interactions between the two rotors are quite strong as shown by Podboy and Krupar,³ generating an important noise over a very large spectrum and in all directions with a high tonality, contrarily to the classical turbofans where the duct around the fan limits the noise propagation for some frequencies and directions. Moreover dedicated liners in the nacelle can reduce the remaining tonal content at the engine inlet and outlet. The rotor interactions can be split into two distinct components. The first one is the tonal emission yielded by the periodic interactions of deterministic flow structures on each rotor. Tonal sources not only includes the impingement of vortical structures such as wakes or tip vortices coming from the front rotor onto the downstream rotor blades, but also the wall pressure fluctuation induced on the front rotor by the potential effects coming from the aft rotor. The second acoustic contribution is the broadband noise generated by the interaction of the random structures of turbulence with the blades and walls. In a CROR, the tonal noise is often the most disturbing feature because of the loud tones dominating a lower broadband noise. The precise understanding of the tonal noise generation and propagation is therefore of prime importance to design future CRORs. This is the focus of the present study.

A first objective is to assess the numerical parameters to predict both aerodynamic performances and aeroacoustic tonal sources accurately. A second goal is to compare two different noise models based on an

*Post-doctorate Student, Mechanical Engineering, Université de Sherbrooke, 2500 Blvd de l'Université, QC, J1K 2R1, Canada; AIAA Member

†Master Student, Mechanical Engineering, Université de Sherbrooke, 2500 Blvd de l'Université, QC, J1K 2R1, Canada

‡Research Associate, Mechanical Engineering, Université de Sherbrooke, 2500 Blvd de l'Université, QC, J1K 2R1, Canada

§Professor, Mechanical Engineering, Université de Sherbrooke, 2500 Blvd de l'Université, QC, J1K 2R1, Canada; AIAA Lifetime Member.

¶PhD, Acoustics engineer, Sneecma - Safran Group, Rond-point René Ravaud - Réau, 77550 Moissy-Cramayel, France

acoustic analogy in free-field, a modified Hanson's model in the frequency domain and an advanced-time formulation of the classical Ffowcs Williams and Hawkings' analogy in the time domain. A third objective is also to check the noise sources at another critical operating condition (approach) than the usual cruise configuration that the CROR has been designed for. The CROR configuration and a summary of the unsteady aerodynamic simulations achieved at approach conditions are first described in the next section II. The two acoustical models are then outlined in section III. Finally the acoustical results are shown in the last section.

II. CROR configuration and aerodynamic simulation

The unsteady flow field for a realistic modern CROR configuration (hub and blade geometries) has been recently achieved.⁴ Yet the latter does not take into account installation effects such as the pylon supporting the engine or the vicinity of the aircraft body or wings. Moreover, the ambient flow is supposed uniform without general incidence relatively to the engine to reproduce the wind tunnel test setup. The simulated configuration is represented in Fig. 1(a), along with the computational domain (transparent surfaces). The aft rotor is clipped in order to reduce the interaction with the wake of the front rotor in cruise conditions. The distance between the two rotors is approximately $2c$, c being the front rotor chord length. The two rotors have B_1 and $B_2 = B_1 - 2$ blades respectively.

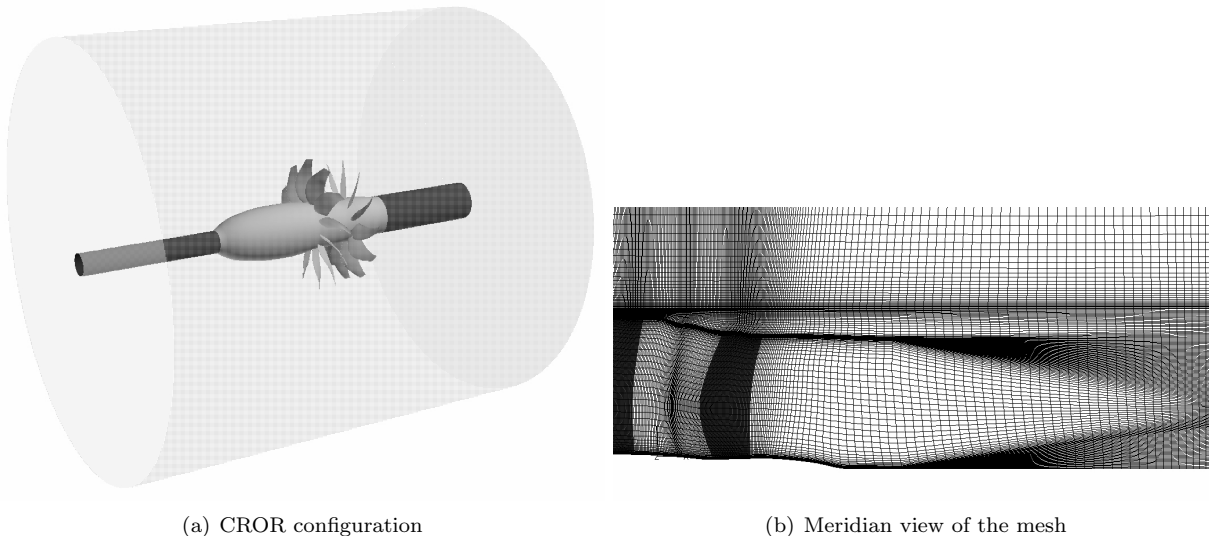


Figure 1. CROR numerical set-up

The study has been performed at approach conditions. The advancing Mach number is about $M_x=0.2$ and the tip relative Mach number for the front rotor is subsonic. For the present design, both rotors rotate at the same speed ($\Omega_1=\Omega_2$), with an quasi-equal torque split. Ambient pressure and temperature are set to $P_s=101325$ Pa, $T_s=303.15$ K respectively. These conditions were chosen because of the importance of noise emission during the take-off and landing phases.

The computational domain is $20c$ long upstream of the front rotor, $15c$ long downstream of the aft one, and the outer diameter is approximatively four times bigger than the front rotor diameter D .

Unsteady Reynolds-Averaged Navier-Stokes (URANS) simulations have been performed using the cell-centered structured solver TurbFlow.⁵ Spatial discretization was performed using the second-order upwind AUSM+-up scheme⁶ with the Van Albada limiter for the conservatives variables (density, momentum and energy), whereas a first order upwind scheme was used for the turbulent flow-field. Kok's two equation k- ω model⁷ is used for turbulence coupled with Menter's turbulence kinetic energy production limiter.⁸ Time discretization is achieved using an explicit second-order 5-steps Runge-Kutta single time-stepping scheme. Using a mesh fine enough to reach a first cell dimensionless height $y^+ = 5$ mandatory for the above turbulence model, there is about 5 million mesh points for the whole case (Fig. 1(b)). Soulard *et al.* showed that, for approach conditions (lower Mach number and Reynolds number based on the rotor chords), this

mesh refinement was enough to yield global performances (thrust, torque and efficiency) and flow features independent of the grid.⁴ Note that Colin *et al.* found for a similar but different CROR configuration that, at take-off, at least 10 millions nodes were needed for resolved chimera and chorochronic URANS simulations.^{9–11} Only on the high-frequency interaction tones ($3BPF_1 + 3BPF_2$), an even finer grid of 30 millions nodes was needed and no grid convergence was even achieved.¹⁰

III. Acoustic models

There are actually several possibilities to calculate the tonal acoustic emissions of a CROR, ranging from simple and fast analytical models to complete but very costly direct numerical simulations. Using an acoustic analogy, the different noise contributions of such a rotating machine can be split into three main contributions : (i) a monopole term caused by the fluid displacement by the blade, (ii) a dipole term coming from the force exerted by the fluid on the blade and (iii) a quadrupole one originating in the fluid turbulence and possible volume sources. Yet, as the considered Mach number is relatively low, both the thickness noise and the quadrupole contribution are neglected here, and only the dipole term is kept.

A. Modified Hanson's model

The first technique that considers counter-rotating dipoles is the semi-analytical model proposed by Hanson.¹² It predicts the far-field acoustic pressure $p(x, r, \theta)$ for any CROR using the dipole source distribution over the blades, and reads in the time domain:

$$\begin{aligned} p(\vec{x}, t) = & \frac{-i\rho a^2 B_2 \sin\theta}{8\pi(r_1/D)(1-M_x \cos\theta)} \sum_{m=-\infty}^{\infty} \sum_{k=-\infty}^{\infty} \exp\left(i(mB_2 - kB_1)(\phi - \phi^{(2)} - \pi/2)\right) \\ & \times \exp(i(mB_2\Omega_2 + kB_1\Omega_1)(r/a - t)) \int_{hub}^{tip} M_r^2 \exp(i(\phi_0 + \phi_s)) \\ & \times J_{mB_2 - kB_1} \left[\frac{(mB_2\Omega_2 + kB_1\Omega_1)z_0(D/(2a))\sin\theta}{1 - M_x \cos\theta} \right] \\ & \times \left[k_x \frac{C_{Dk}}{2} \Psi_{Dk}(k_x) + k_y \frac{C_{Lk}}{2} \Psi_{Lk}(k_x) \right] dz_0 \end{aligned} \quad (1)$$

where

$$k_x = \frac{D/a}{M_r} \left[\frac{mB_2\Omega_2 + kB_1\Omega_1}{1 - M_x \cos\theta} - kB_1(\Omega_2 + \Omega_1) \right] c/D \quad (2)$$

$$k_y = -\frac{2}{M_r} \left[\frac{(mB_2\Omega_2 + kB_1\Omega_1)M_T \frac{D}{2a} z_0 \cos\theta}{1 - M_x \cos\theta} - \frac{(mB_2 - kB_1)M_x}{z_0} \right] c/D \quad (3)$$

$$\phi_s = \frac{D/a}{M_r} \left[\frac{mB_2\Omega_2 + kB_1\Omega_1}{1 - M_x \cos\theta} - kB_1(\Omega_2 + \Omega_1) \right] \frac{\text{MCA}}{D} \quad (4)$$

$$\phi_0 = \frac{2}{M_r} \left[\frac{(mB_2\Omega_2 + kB_1\Omega_1)M_T \frac{D}{2a} z_0 \cos\theta}{1 - M_x \cos\theta} - \frac{(mB_2 - kB_1)M_x}{z_0} \right] \frac{\text{FA}}{D} \quad (5)$$

In Eqs. (4) and (5) MCA and FA are offsets representing the sweep and lean of the blade respectively. Aside from the geometric definition of the configuration, the inputs of the model are the unsteady blade load distributions along the chord, expressed as an integral lift/drag coefficient $C_{L/Dk}$ multiplied by a normalised distribution $\Psi_{L/Dk}$. In its original formulation, Hanson considered that the pressure variation along the chord was in phase, thus neglecting the time lag induced by the propagation of the flow structure along the blade. This was corrected here by expressing the distribution $\Psi_{L/Dk}$ as complex values. In this study, the harmonic pressure distribution over the blades are extracted from the unsteady numerical simulation. The extended Hanson's model has been compared with the analytical model recently proposed by Carazo *et al.*¹³ The same overall Overall Sound Pressure Level (OASPL) and reasonable agreement on the tonal directivities was found by Soulard *et al.* given the uncertainty on the blade loading distribution.⁴

B. Ffowcs-Williams and Hawkings's analogy

In the second method, the far-field acoustics is obtained from the near-field unsteady conservative variables by a classical Ffowcs Williams and Hawkings' (FWH) analogy. An extension of the code *Foxhawk* originally developed by Casalino¹⁴ is used for the present study. Its formulation is based on the forward-time formulation for moving observers developed by di Francescantonio¹⁵ on porous integration surface. It enables to perform on-the fly acoustic calculations. On the contrary, a retarded-time approach would need the complete sampling of the solution to perform the acoustic extrapolation. For a fixed observer at $\vec{x} = (x_1, x_2, x_3) = (x_i)$, this yields the following expressions for the far field acoustic pressure:

$$4\pi p(\vec{x}, t) = \frac{1}{c_0} \int_S \left[\frac{\dot{F}_r}{r(1-M_r)^2} \right]_{\text{ret}} dS + \int_S \left[\frac{F_r - F_M}{r^2(1-M_r)^2} \right]_{\text{ret}} dS + \frac{1}{c_0} \int_S \left[\frac{F_r (\dot{r} M_r + c_0 (M_r - M^2))}{r^2 (1-M_r)^3} \right]_{\text{ret}} dS \quad (6)$$

where \vec{F} is the pressure force acting on the surface S . F_M is this force projected in the source movement direction. Only results from solid surface sources are presented below.

IV. Results

A. Flow-field analysis

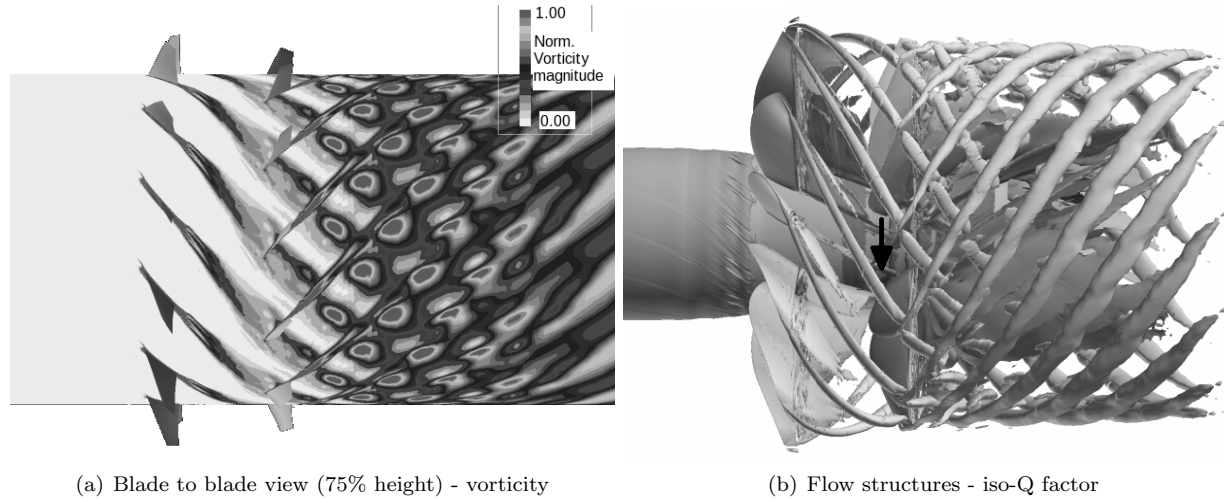


Figure 2. Noise for both meshes

For the considered approach condition, there is a contraction of the streamlines downstream of each rotor (“vena contracta” at approach), but without any flow separation on the blades. Moreover, given the torque balance between the two rotors and the clipping of the second rotor, the aerodynamic load is higher on the aft blades. The second rotor operates properly, and reduces the swirl generated by the front rotor. Yet, an important positive swirl downstream the tip region of the aft rotor is generated corresponding to the aft tip vortex.⁴

The unsteady flow structures over most of the blade span are mainly characterised by the wake impingement of the front rotor on the aft rotor. A vorticity map in a blade to blade section clearly reveals the classical “chopping” of the front wakes by the aft blades (Fig. 2(a)). When convected downstream, the front wakes progressively merge with the aft wakes yielding the checkerboard pattern observed downstream. As pointed out by the grid study of Soulat et al.,⁴ the present fine simulations are accurate enough to properly propagate these flow patterns far downstream. It should also be emphasized that for these particular

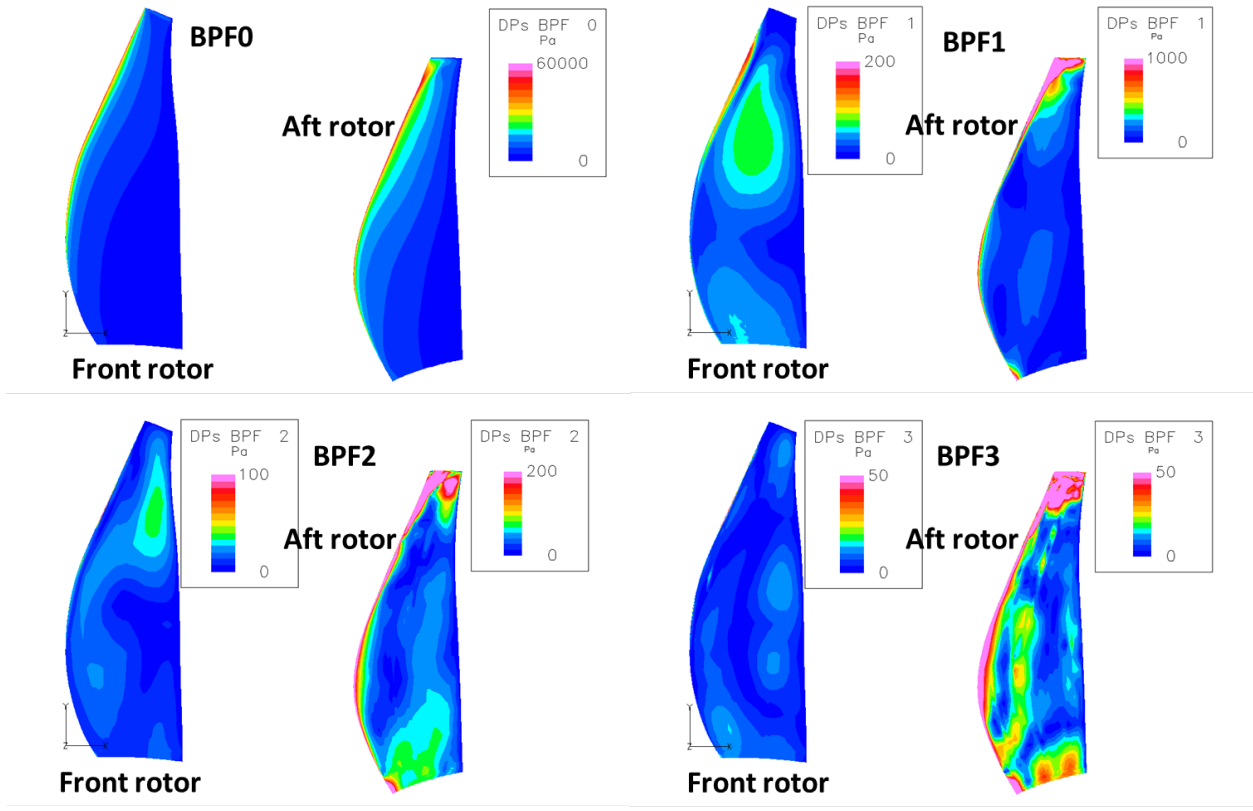


Figure 3. Dipolar source distribution over the blades. Harmonics ranked from 0 to 3

approach conditions, the wakes of both rotors are almost perpendicular and that any RANS simulation (frozen-rotor or mixing plane) would yield unphysical flow patterns in the aft rotor passage and downstream the CROR, which may question any performance prediction on the aft rotor with a steady approach.

The flow topology is also dominated by several strong vortical structures. Besides the front-rotor wake, the most important ones are the two tip vortices generated by the rotors. In Fig. 2(b), iso-surfaces of the Q-criterion reveal that the tip vortex coming from the front rotor impinges on the second rotor at approximately 87% of the span. This is to be contrasted with the results of Colin *et al.* at take-off conditions, which showed that the rear rotor cropping (similar to the present CROR) was sufficient to prevent the front-rotor tip vortex from interacting with the aft blade.¹¹ An additional strong noise source is thus expected at approach. As for the viscous wake in Fig. 2(a), the front-rotor tip vortex is thus chopped, but the resulting pieces keep some vortical structures as illustrated by the small patches of iso-Q surfaces visible downstream of the aft rotor. The aft tip vortex is even bigger and stronger, which is consistent with the higher load on this rotor. It initially has a wavy trajectory induced by the remainings of the front-rotor tip vortex travelling below it. It becomes a thick vortex sheet further downstream when all the front and aft tip vortex cores merge. The strength of this vortex sheet could be an additional strong noise source when interacting with the downstream empennage depending on the CROR installation on the plane. Finally, a significant horseshoe vortex developing on the front rotor induced by the boundary layer developing on the long hub, outlined by an arrow in Fig. 2(b), is mainly visible on the suction side of the blades. Although it decreases quite rapidly and completely disappears after impinging the aft blades, the vortex is still visible up to the leading edge of the second rotor and causes a third strong interaction with the aft rotor blade.

B. Noise source analysis

An accurate determination of the acoustic sources is of prime importance for a correct noise prediction. Interestingly, the harmonic load distributions e.g. the sources, have to be determined for noise prediction

using Eqs. (1-3), and are therefore directly available. The first four loading harmonics, thereafter noted 0BPF, 1BPF, 2BPF and 3BPF are presented in Fig. 3 for each rotor blade. The frequencies used for the harmonic decomposition are the blade passing frequency (BPF) and following sub-harmonics ($kB_1\Omega_1 + mB_2\Omega_2$, $\forall k, m$). Load harmonic 0BPF is the steady loading of the blade. Although constant, 0BPF is responsible for the rotor loading noise at frequencies $kB_{1/2}\Omega_{1/2}$, $\forall k$ because of the unsteadiness introduced by the blade movement. Soulard *et al.* showed that all higher harmonics had the same shape and order of magnitude as the third harmonics 3BPF.⁴ Grid independence was also shown on the fine grid for these first harmonics. This is consistent with the harmonic decay found by Colin *et al.* at take-off conditions, where they showed similar low, almost constant levels beyond the third loading harmonics (Fig. 13).⁹

As expected, the steady loading 0BPF is mainly concentrated near the leading edge of each blade, and the aft rotor loading is higher than the front one. Moreover, the amplitude of the steady loading is a hundred times larger than the following loading harmonics.

Considering the first truly unsteady load harmonic (1BPF), the maximum pressure fluctuation over the aft rotor is about ten times stronger than on the front rotor. This confirms that the wake and vortex impingement on the aft blade are far more energetic than the interaction of the potential effects with the front rotor. The fluctuations on the aft rotor are located mainly near the leading edge, except in the root and tip regions. This suggests that the wake intensity decreases quickly after the impingement, which is consistent with analytical models such as those of Sears^{16,17} and Amiet,¹⁸ and numerical results obtained at take-off by Colin *et al.* (Fig. 11).⁹ The effects of the front tip vortex are particularly clear here, maximising the pressure fluctuation above 80% of the span. The tip vortex interaction is also responsible for a spread of the pressure fluctuations over the whole chord in the tip region. The impact of the small horse-shoe vortex is also visible, with another strong fluctuation-increase near the blade root. Although weaker (maximum pressure fluctuation five times weaker), the potential effects on the front blade are not negligible either. The unsteady loading topology is somehow different for this rotor, with a better spread of the fluctuations all over the blade surface. The maximum fluctuation is located in the upper half of the blade, at mid-chord. At the hub, the horse-shoe vortex developing from the front blade leading edge provides the fluctuations seen at the blade foot.

The fluctuations associated with the second loading harmonic 2BPF are decreasing progressively compared to 0BPF and 1BPF. Again, the levels seen on the aft rotor remain much higher than on the front rotor, and the potential effects are still visible on the front blade. The topology on the front rotor is slightly different from the one observed for 1BPF, with the maximum fluctuations located above 60% span, near the blade trailing edge. The global topology on the aft rotor is the same, but some small differences appear. The impact of the tip vortex now generates a maximum fluctuation near the leading edge only, quickly decreasing along the chord.

The rotor-rotor interactions can be traced up to the third order for the aft rotor and to the second order for the front one. Nevertheless, Soulard *et al.* noted that the impacts of the vortices on the aft blades are still clearly visible up to 5BPF, confirming that these interaction-mechanisms are probably the most effective from an acoustical point of view.⁴ These loading harmonics then provide the far-field acoustic pressure shown in the next section.

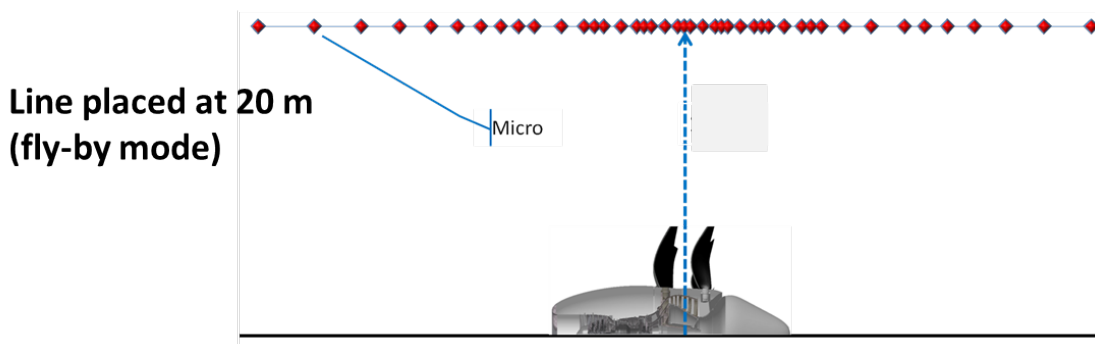


Figure 4. Acoustic experimental set-up.

C. Acoustic parameter sensitivity

To assess the quality and the robustness of each model, the impact of parameters such as mesh refinement, data sampling and number of blade passing periods required is studied for both models. All directivities are considered as in the NASA experiment, which corresponds to a linear array of microphones as in the fly-by mode shown in Fig. 4.

First the comparison in Fig. 5(a) shows that the mesh refinement has a strong effect in terms of OASPL for the extended Hanson's model but the directivity patterns are preserved. Less effect is seen on the FWH computations. On the contrary, for the FWH computations the mesh coarsening has a greater impact on the interaction tones. A huge difference in levels of the minima for the mode $2BPF_1 + 2BPF_2$ in Fig. 5(b) is clearly visible. When moving to the finer mesh (8 million nodes), Soulat *et al.* noted that the OASPL were unchanged and that only small differences in the minima (2-3 dB) were observed.⁴ This is consistent with the differences observed by Colin *et al.* at take-off when they varied both the mesh topology and the grid refinement (Figs. 11 and 16 respectively).¹⁰ All the consequent simulations have then been achieved on the fine grid (5 million nodes).

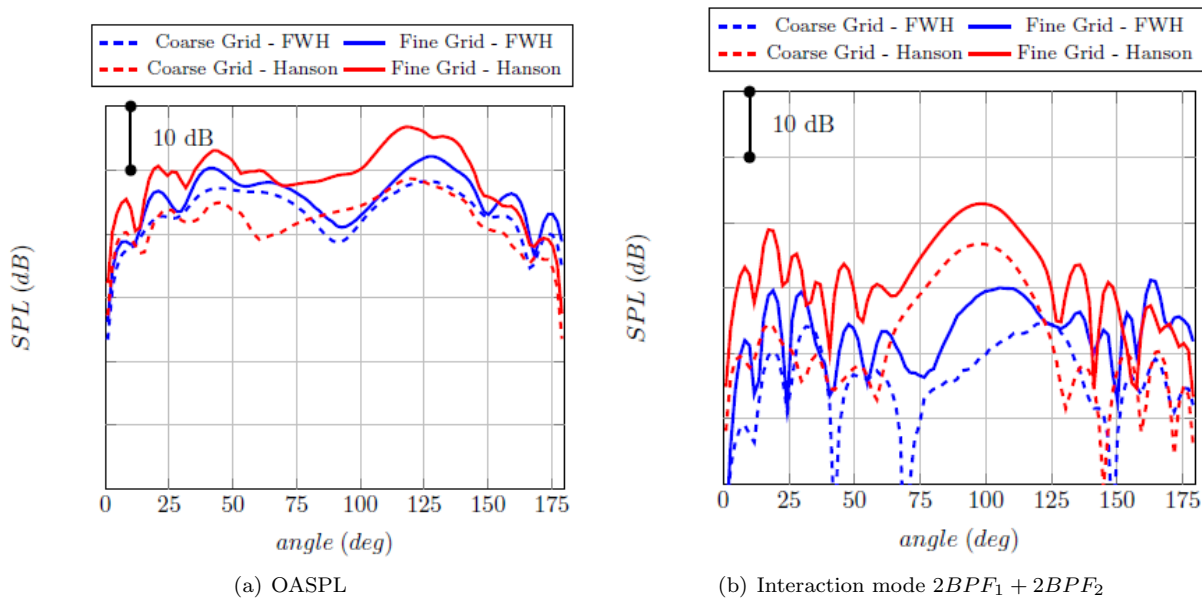


Figure 5. Effect of the grid size on CROR tonal noise.

Another fundamental parameter is the choice of the time discretization for the models that is linked to the number of aerodynamic solutions needed for each Blade Passing Period (BPP). Initial computations used a time-step of 75 samples per blade passing period. This choice allowed achieving reasonable computation times for Hanson's model and the solid FWH formulation. However, the computations on the porous surface were particularly slow, which triggered the study of the sampling reduction. The reduction of the sample yields an important decrease of the computational time but, as shown in Fig. 6, the effects on levels and directivity are too significant to reduce the sampling rate. This should be related to the recent study by Cunha and Redonnet.¹⁹ All the consequent simulations have been achieved with 75 samples per blade passing period.

The last studied parameter is the number of blade passing periods itself. It triggers some major differences between the two approaches. A good convergence is achieved with only four blade passing periods for Hanson's model as shown in Fig. 7. Both OASPL and directivity for the low-frequency BPF_2 tone are converged. Similar results are achieved for all interaction modes. On the contrary, the FWH computations seem to require much more blade passing periods to resolve the phase information along the blade correctly. From twelve blade passing periods the OASPL is converged but the low-frequency tones have still important variations (Fig. 7). For instance, the low-frequency tone BPF_2 shown in Fig. 7(b) has large spurious side-lobes for low BPP with a minimum where both Hanson's numerical result and experimental data have a maximum. Only a much longer time record (beyond 12 BPP) yields the expected correct large lobe centered

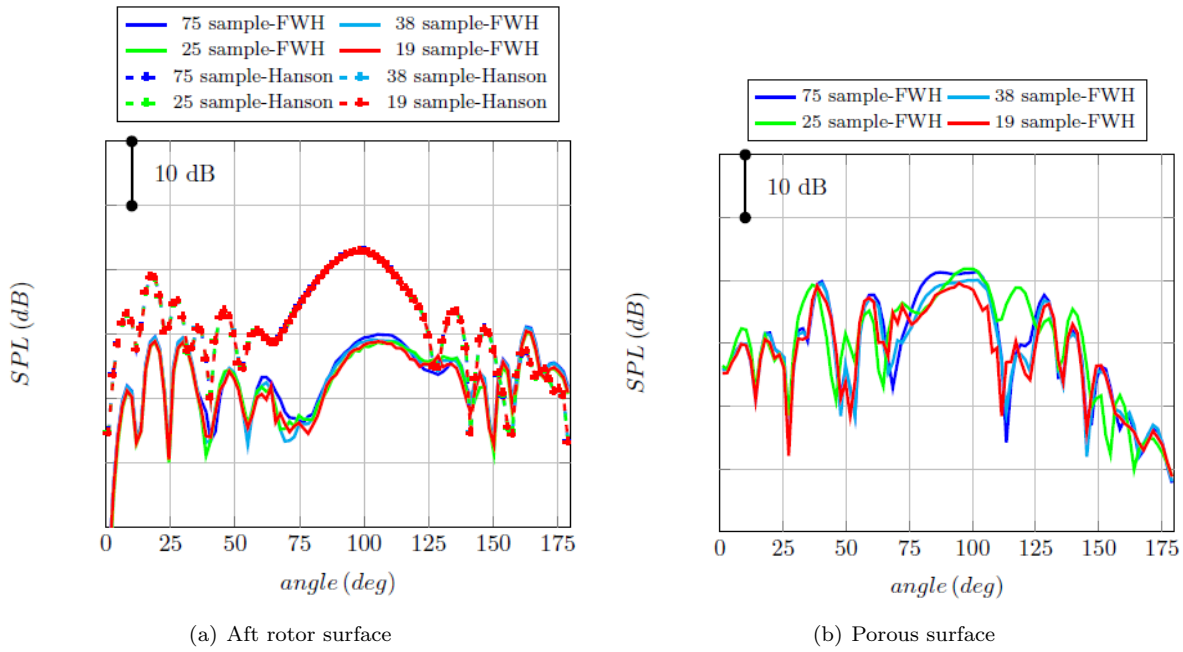


Figure 6. Data sampling for $2BPF_1 + 2BPF_2$

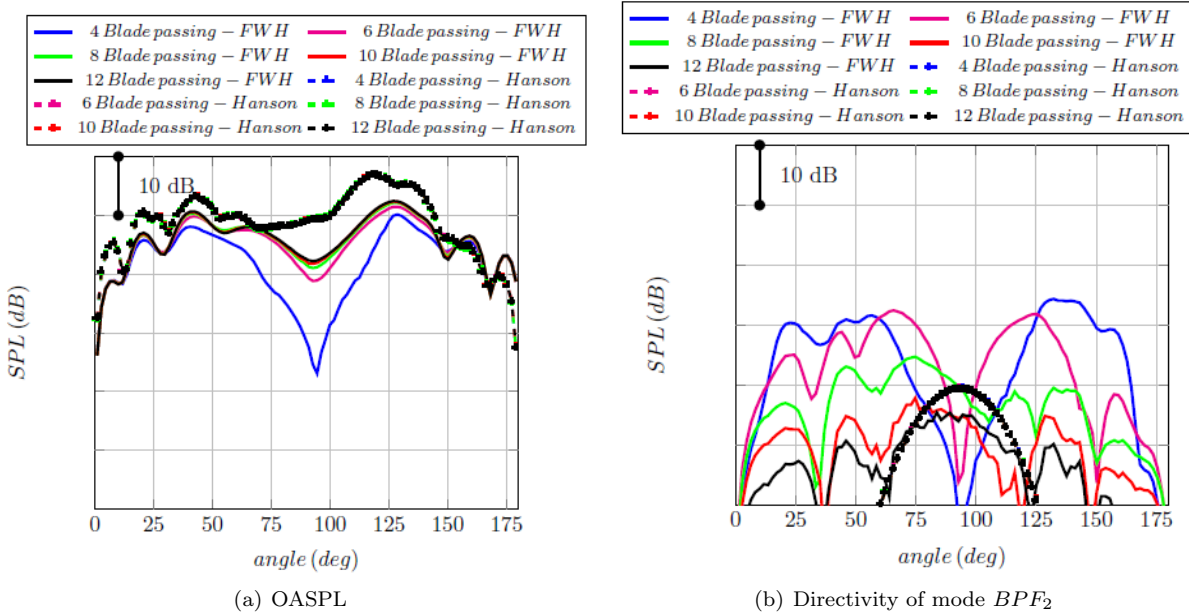


Figure 7. Convergence with the number of blade passing periods (BPP).

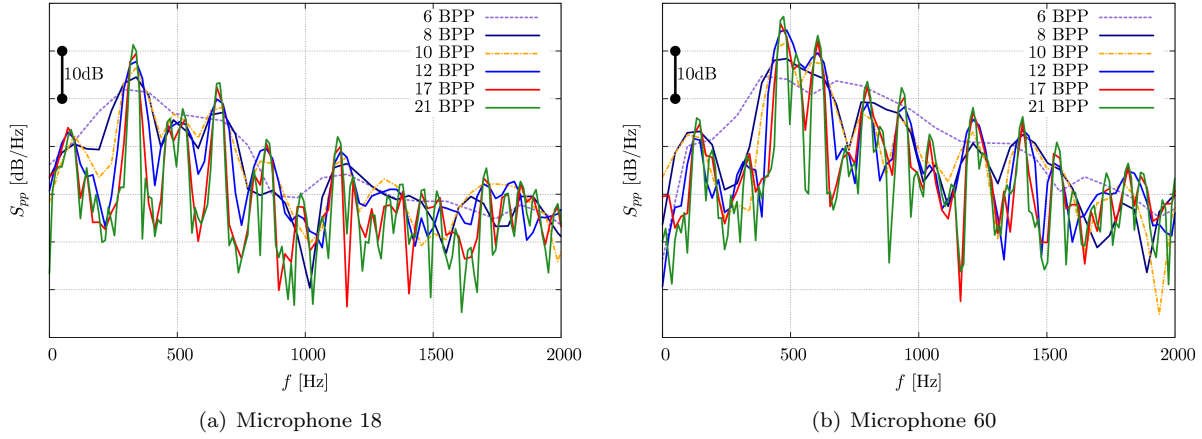


Figure 8. Convergence of far-field acoustic spectra for the B_1 - B_2 CROR configuration.

around 90°, and even with 21 BPP the side-lobes have not yet completely disappeared. Moreover, the spectra at given positions for the actual B_1 - B_2 CROR configuration in Fig. 8 clearly show that the longer the time record is (and consequently the smaller the frequency resolution is), the more tones are resolved, which is key for CROR tonal noise prediction. Again even with 21 BPP which frequency resolution is 12 Hz, the two selected microphones show that new tonal peaks corresponding to interactions tones start being captured. Therefore, additional periods still need to be run to properly resolve some of the interaction tones.

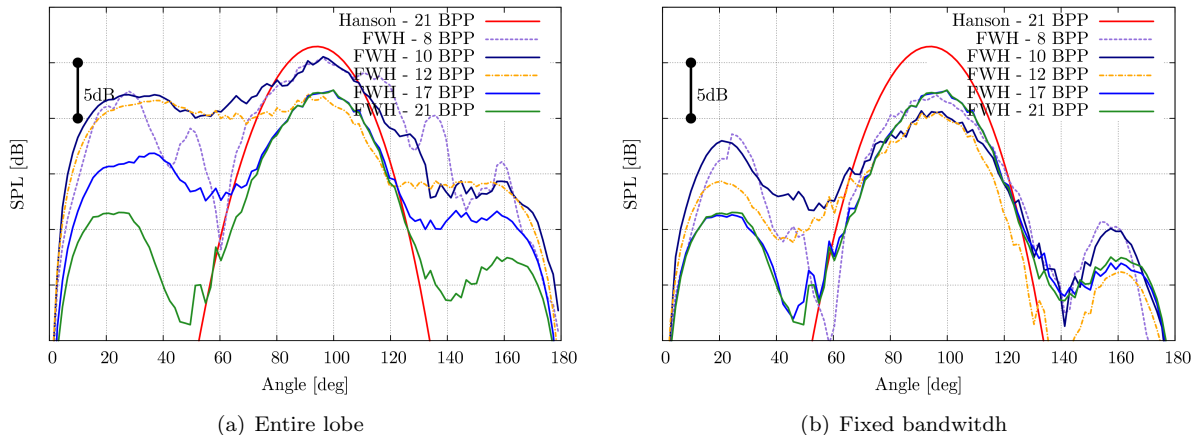


Figure 9. Convergence of directivity of mode BPF_2 with the number of BPP.

Finally, the directivities of the tones in Figs. 5-7 have been obtained by selecting the peak value close to the selected frequency of a tone. An alternative method consists in integrating the whole peak provided it can be distinguished. Such a procedure can only be done for the BPF_2 tone beyond 8 BPP, which already explains the unphysical directivity observed in Fig. 7(b) below this simulation duration. An uncertainty then arises on how wide a frequency range a peak should be integrated on. Two different methods are illustrated in Fig. 9. First each tone/hump can be integrated over its entire range depending on the number of BPP (larger range for less resolved lower BPP). This yields the directivity plot shown in Fig. 9(a). The maximum of the lobe at about 100° then converges in 12 BPP even though the side lobes remain large even at 21 BPP. The second method consists in selecting the frequency range of 21 BPP for which the tone is properly resolved and applying this fixed bandwidth to the other shorter duration simulations. Fig. 9(b) clearly shows that the main lobe now converges almost immediately and that the side lobes are significantly reduced even at 12 BPP. Yet, this requires to know a priori how many BPP are needed to resolve properly a tonal peak, and therefore cannot be practically applied (an a posteriori method). Nevertheless, the integration method is now preferred and is used for the spectral comparisons with experiment shown below.

D. Comparison of the acoustic models on a B_1 - B_1 configuration

This section focuses on the results with both acoustic models for the B_1 - B_1 geometry which flow field has been computed. In Fig. 10, the spectrum obtained with FWH analogy shows a good agreement for the position of all BPF and harmonics. With the increase of the blade passing periods, the low frequency range is better converged and the tonal peaks are becoming sharper and more and more accurate, and all harmonics are resolved. For this CROR configuration, 21 BPP seem to yield an almost time convergence of the spectra (except at a few minima that do not contribute significantly to the noise level). This is to be contrasted with the actual B_1 - B_2 configuration shown in Fig. 8. Both sets of spectra show however that at least 10 BPP are necessary to capture the main tones and provide a sensible peak integration, and that all the tones (pure and interaction) and consequently the OASPL exhibit a strong directivity.

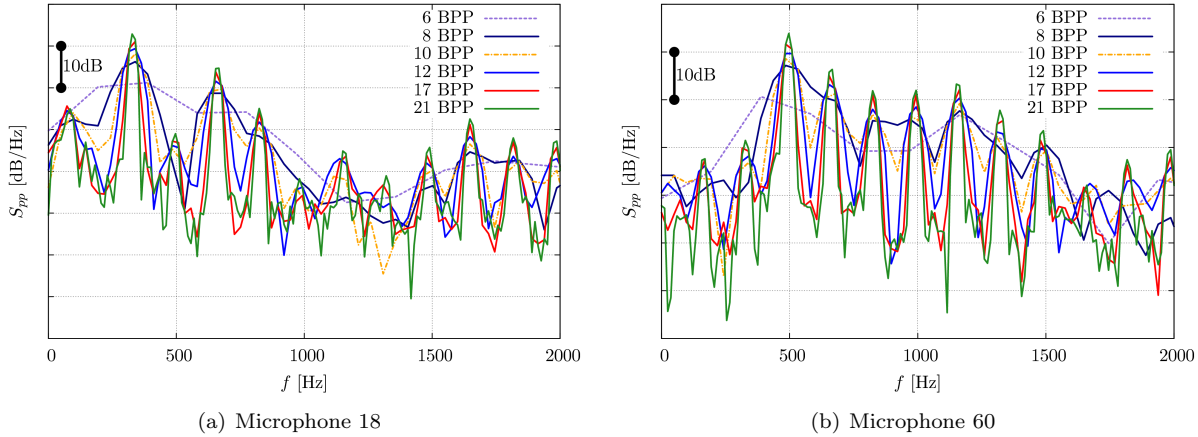


Figure 10. Convergence of far-field acoustic spectra for the B_1 - B_1 CROR configuration.

This strong directivity is confirmed in Fig. 11 for the B_1 - B_1 configuration using both acoustic models. For the directivity for all frequencies (OASPL) or for particular frequencies (interaction tonal modes), both models give the same trend in terms of level and shape. The difference in directivity for the OASPL and the first two harmonics is less than 5dB. The discrepancies for the higher harmonics $3 * BPF_1$ and $4 * BPF_1$ are clearly larger. The inputs on both models are identical so these differences could only come from the low resolution of the spectrum in the FWH calculations at low frequency and possibly from an insufficient sampling rate at high frequencies for both methods.

E. Comparison and validation of the acoustic models on a B_1 - B_2 configuration

In this section the noise radiated by the tested configuration with a reduced number of blades to $B_2 = B_1 - 2$ for the rear rotor is studied. In fact, both acoustic post-processing methods allow the choice of the number of blades for the rear rotor based on the same acoustic sources coming from the above URANS simulations. Soulard *et al.* had already made preliminary comparisons with the results of Schnell *et al.*^{4,20} The present configuration is indeed close to another CROR tested at DLR in similar flight conditions. Compared to the experimental and numerical results obtained at DLR/TsAGI, the current study predicted the directivity of the CROR fairly well for the two interaction tones $BPF_1 + BPF_2$ and $2 * BPF_1 + 2 * BPF_2$. The only differences were an increased number of lobes for $\theta \geq 100^\circ$ and slightly more amplitudes of the dips. These discrepancies were attributed to a slightly different blade loading.

The numerical results are here compared with the experimental data obtained on the present configuration, during the ORPR tests in the NASA LSWT wind tunnel. In Fig. 12 the prediction of Hanson's model are in good agreement with the measurements for all tones both in terms of levels and shape. For the $BPF_1 + BPF_2$ tone, the only major difference seems to be around 30° where the model overestimates the level and has an extra lobe. Yet, the results of the FWH computations are very similar suggesting that it might come from the numerical prediction of the blade loading or some spurious installation effect in the experiment. For the second interaction mode $BPF_1 + 2 * BPF_2$ both acoustic methods agree fairly well with the measurements. Yet, there is a slight off-set of the radiation lobe around $40-50^\circ$ between the two

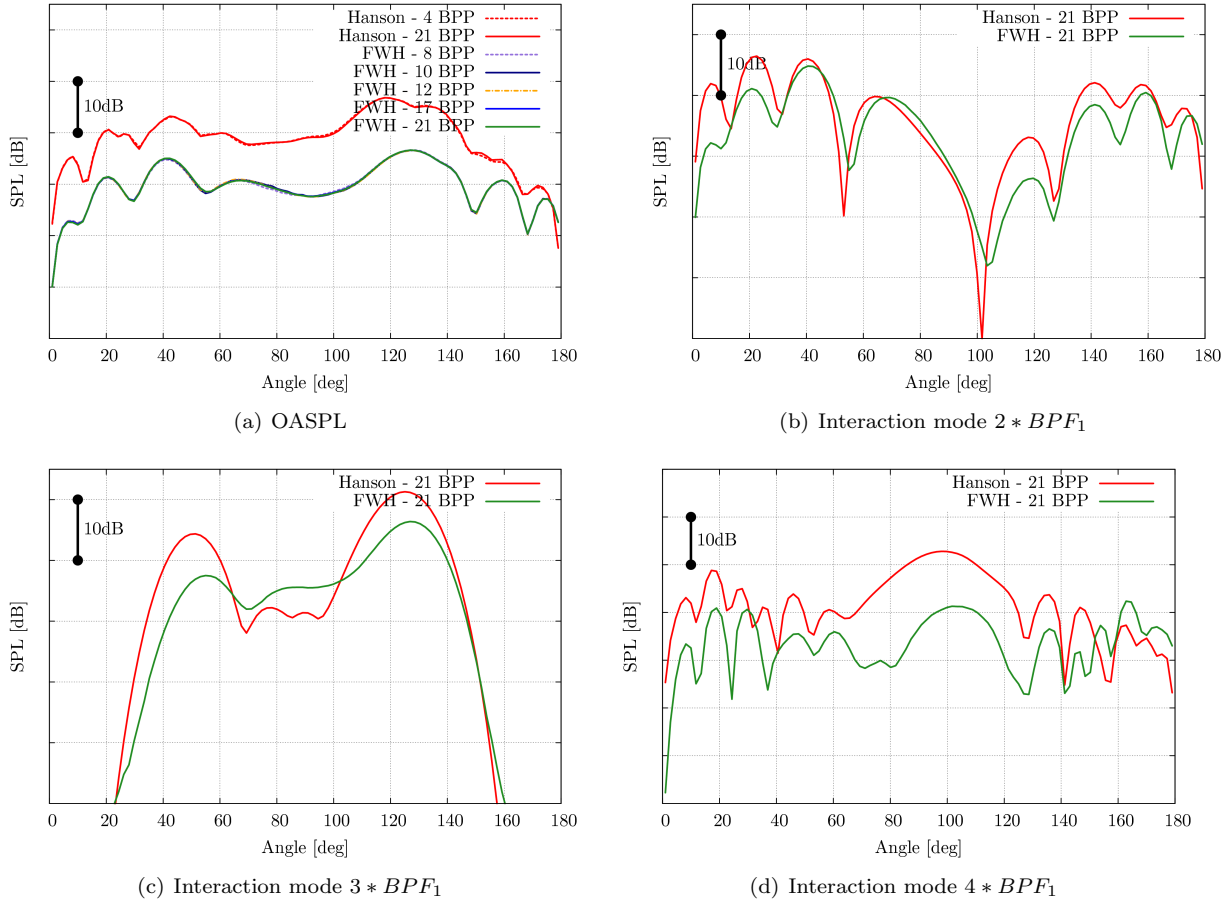


Figure 11. Comparison FWH - Hanson on a B_1 - B_1 configuration for 21 blade passing periods.

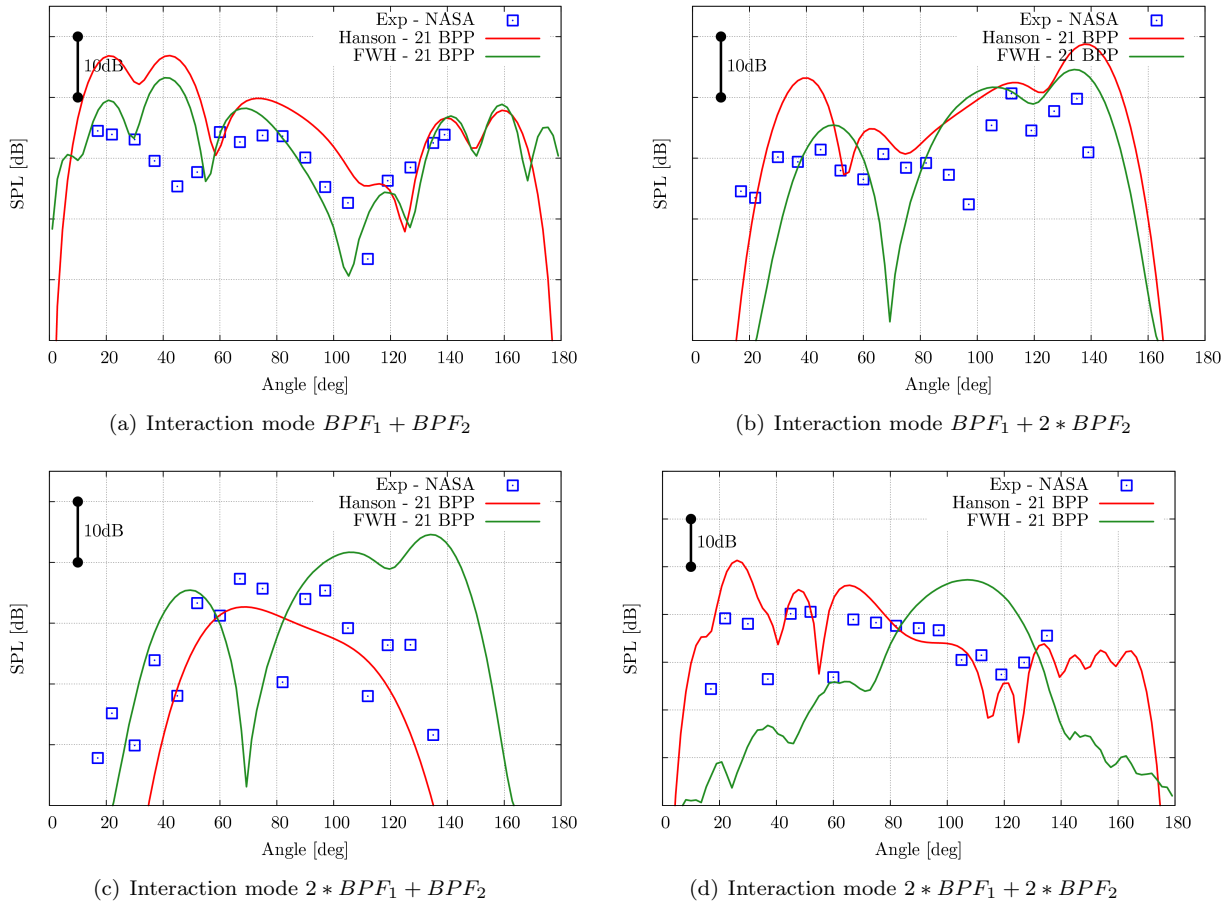


Figure 12. Comparison FWH - Hanson -Experiments on a B_1 - B_2 configuration.

simulations that the experimental data can hardly resolve. The main discrepancy is however around 100° where no dip is seen in Hanson's calculation and a much sharper dip is found around rather 70° in the FWH calculation. For the third interaction mode $2 * BPF_1 + BPF_2$, the time resolution is not yet enough to resolve this peak in the FWH calculation and therefore the same directivity as for $BPF_1 + 2 * BPF_2$ is obtained. On the contrary, Hanson's prediction recovers the levels and its shape goes through the experimental scatter (sign of the difficulty to isolate this tone). For the highest-frequency interaction tone $2 * BPF_1 + 2 * BPF_2$, the numerical prediction with Ffowcs Williams and Hawkings' analogy only recovers the levels in the range $60\text{--}140^\circ$ with a slow improvement with additional BPP. Hanson's prediction yields the correct shape and levels suggesting that the source predictions are accurate and time convergence might indeed be the issue. Colin *et al.* also recovers this interaction tone by a FWH calculation but with a larger simulation time (Fig. 16)¹⁰ but on a slightly different CROR configuration ($B_2 = B_1 - 3$).

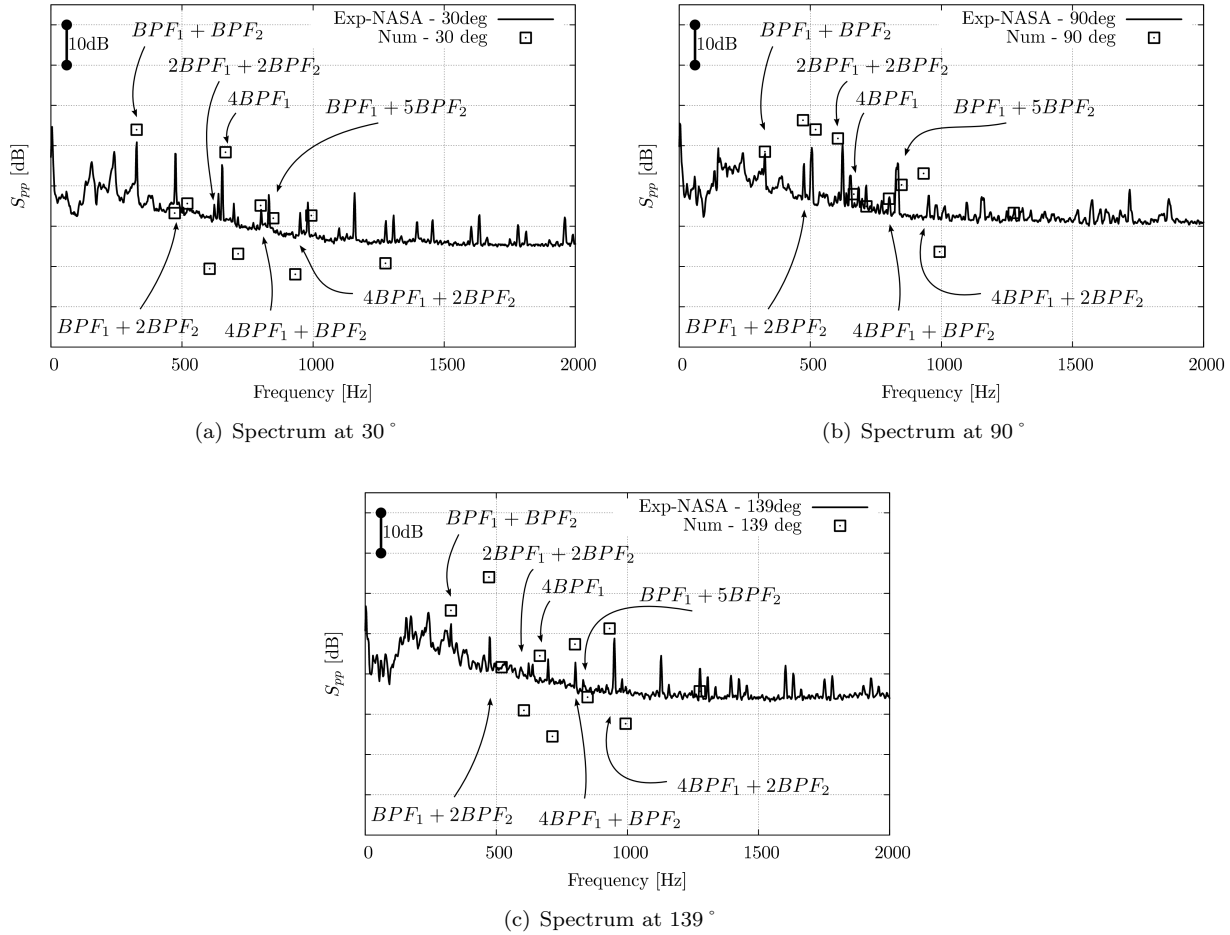


Figure 13. Comparison of far-field FWH acoustic spectra with NASA measurements.

To further check this, current FWH spectra at 21 BPP are compared in Fig. 13 with the measured spectra for three different microphone positions at 30° , 90° and 139° respectively. The harmonics $4 * BPF_1$ and the interaction mode $BPF_1 + BPF_2$ have the correct levels in all directions. Some higher-frequency interaction tones such as $2 * BPF_1 + 2 * BPF_2$, $4 * BPF_1 + BPF_2$ and $BPF_1 + 5 * BPF_2$ have also proper levels in most directions. The best predicted overall spectrum is at 90° . As already mentioned, further computational time will bring some improvement to the current prediction especially for the interaction tones that are hardly resolved at 21 BPP such as $2 * BPF_1 + BPF_2$ and $BPF_1 + 2 * BPF_2$.

Finally the directivities of the OASPL and a few tones (BPF_1 , $BPF_1 + BPF_2$ and $2 * BPF_1 + 2 * BPF_2$) are compared for both rotors by applying the FWH method to each rotor separately in Fig. 14. Consistently with the analysis of the noise sources (wall-pressure fluctuations) in Section IV.B, the aft rotor has a much larger contribution and its OASPL is about 20 dB louder than the front rotor in all directions. It has a similar

steady loading noise (split torque between the two rotors) but a much larger unsteady dipolar noise for all tones in almost all directions. Only at limited locations (around 155° for instance), the $2 * BPF_1 + 2 * BPF_2$ tone of the front rotor is larger than the similar contribution of the aft rotor. Consequently it can be concluded that at approach conditions, the aft rotor in a typical clipped CROR is the dominant noise source.

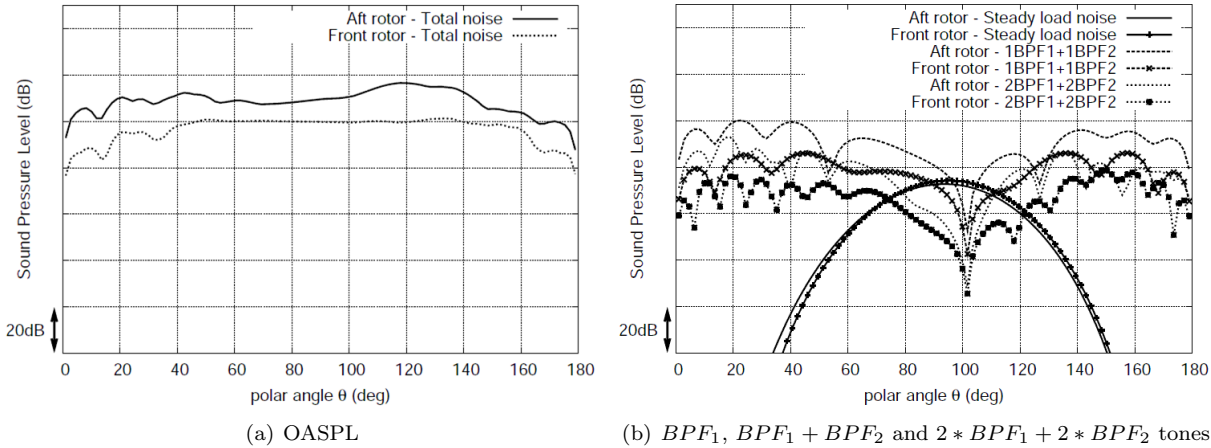


Figure 14. Comparison of far-field FWH acoustic spectra for the front and aft rotors.

V. Conclusions

A hybrid method combining a three-dimensional unsteady RANS simulation and two acoustic analogies has been successfully applied to a realistic clipped CROR at approach conditions. The first analogy is an advanced-time formulation of the Ffowcs-Williams and Hawkings' analogy. The second one is a frequency formulation of the Ffowcs-Williams and Hawkings' analogy, originally developed by Hanson and extended to non compact chord length. The unsteady simulation has been achieved for a $B_1=B_2$ configuration on one sector but the noise predictions have been achieved for both $B_2=B_1$ and $B_2=B_1-2$ rear rotor blades.

The unsteady flow field shows several strong vortical structures, namely the wakes of both rotors, the horse-shoe vortex at the blade root of the front rotor and the strong tip vortices of both rotors. The unsteady blade loading on the cropped aft-rotor consequently show three zones of strong interaction: the tip region is strongly affected by the impact of the front-rotor tip vortex caused by the vena contracta at approach condition; the hub region also shows the strong impact of the horse-shoe vortex formed on the front-rotor; finally the rest of the blade exhibits strong fluctuations caused by the impact of the front-rotor wake. All these pressure fluctuations are however concentrated at the leading edges of the rear blades. The flow analysis also shows some significant potential effect of the aft rotor on the front front. Finally the strength of the tip vortex of the rear-rotor caused by the high loading of the cropped blade yield a strong vorticity layer that could cause a secondary noise source by impingement on some downstream empennage or some strong contrail vortices.

The implementation of the frequency acoustic model has been successfully compared with a model recently developed by Carazo *et al.*¹³ Consistent results have also been obtained with acoustic measurements on similar configurations performed at DLR.²⁰ The mesh is seen to have a major impact on the acoustic levels and directivity shape predicted by the method, and a mesh of at least 5 million points should be used that properly resolved the boundary layers on both rotors and the rotor wake interaction. The acoustic signature also confirms the different noise sources identified in the unsteady flow analysis and shows a dominant contribution of the aft rotor acoustic radiation. Very good agreement is achieved for both acoustic models with NASA measurements on the present B_1-B_2 CROR configuration at approach conditions even though the FWH approach would still require more simulation time than the current 21 BPP to properly resolve some interaction tones. Yet, the spectral comparisons with experiment are very favorable especially at 90° from the CROR. Finally, it should be stressed that from a design point of view, the modified Hanson's model seems to be much more computationally efficient as it requires far less blade passing periods (and therefore URANS computational time) to time converge and yield the proper tonal directivities.

Acknowledgments

We wish to acknowledge the financial support of Snecma - Safran Group, the technical support from Fluorem on Turb'Flow, and Compute Canada and the RQCHP (Réseau Québécois de Calcul Haute Performance) for providing the necessary computational ressources.

References

- ¹M'Bengue, L., "Towards ACARE 2020 : Innovative engine architectures to achieve the environmental goals," *27th International Congress of the Aeronautical Science*, Nice, France, 2010.
- ²Woodward, R., "Noise of a model high speed counterrotation propeller at simulated takeoff/approach conditions (F7/A7)," Tech. Rep. NASA-TM-100206, NASA, 1987.
- ³Podboy, G. and Krupar, M., "Laser velocimeter measurements of the flowfield generated by an advanced counterrotating propeller," Tech. Rep. NASA-TM-01437, NASA, 1989.
- ⁴Soulat, L., Kernemp, I., Moreau, S., and Fernando, R., "Numerical assessment of the noise emission of Counter-Rotating Open Rotors," *10th European Conference on Turbomachinery Fluid Dynamics and Thermodynamics*, No. 210, Lappeenranta, Finland, 2013.
- ⁵Caro, J., Ferrand, P., Aubert, S., and Kozuch, L., "Inlet conditions effects on tip clearance vortex in transonic compressor," *Proceedings of 5th European Conference on Turbomachinery Fluid Dynamics and Thermodynamics*, Prague, 2003.
- ⁶Liou, M., "A Sequel to AUSM, PART II: AUSM+-up for all Speed," *J. Comp. Phys.*, Vol. 214, 2006, pp. 137–170.
- ⁷Kok, J., "Resolving the dependence on free-stream values for the k- ω turbulence model," *AIAA J.*, Vol. 38, No. 7, 2000, pp. 1292–1295.
- ⁸Menter, F. R., "Zonal two equation k- ϵ turbulence models for aerodynamic flows," *23rd Fluid Dynamics, Plasmadynamics, and Lasers Conference*, No. AIAA Paper 93-2906, Orlando, FL, USA, 1993.
- ⁹Colin, Y., Carazo, A., Caruelle, B., Node-Langlois, T., and Parry, A., "Computational strategy for predicting CROR noise at low-speed Part I: review of the numerical methods," *18th AIAA/CEAS Aeroacoustics Conference*, No. AIAA paper 2012-2221, Colorado Springs, CO, USA, 2012.
- ¹⁰Colin, Y., Blanc, F., Caruelle, B., Barrois, F., and Djordjevic, N., "Computational strategy for predicting CROR noise at low-speed Part II: investigation of the noise sources computation with the chorochronic method," *18th AIAA/CEAS Aeroacoustics Conference*, No. AIAA paper 2012-2222, Colorado Springs, CO, USA, 2012.
- ¹¹Colin, Y., Caruelle, B., and Parry, A., "Computational strategy for predicting CROR noise at low-speed Part III: investigation of noise radiation with the Ffowcs-Williams Hawkings analogy," *18th AIAA/CEAS Aeroacoustics Conference*, No. AIAA paper 2012-2222, Colorado Springs, CO, USA, 2012.
- ¹²Hanson, D., "Noise of Counter-rotation Propellers," *Journal of Aircraft*, Vol. 22, No. 7, 1985, pp. 609–617.
- ¹³Carazo, A., Roger, M., and Omais, M., "Analytical Prediction of Wake-Interaction Noise in Counter-Rotation Open Rotors," *17th AIAA/CEAS Aeroacoustics Conference/32nd AIAA Aeroacoustics Conference*, 2011, AIAA 2011-2758.
- ¹⁴Casalino, D., "An Advanced Time Approach for Acoustic Analogy Predictions," *J. Sound Vib.*, Vol. 261, No. 4, 2003, pp. 583–612.
- ¹⁵Francescantonio, P. D., "A New Boundary Integral Formulation for the Prediction of Sound Radiation," *J. Sound Vib.*, Vol. 202, No. 4, 1997, pp. 491–509.
- ¹⁶Karman, T. V. and Sears, W. R., "Airfoil theory for non-uniform motion," *J. Aeronautical Sciences*, Vol. 5, No. 10, 1938, pp. 379–390.
- ¹⁷Sears, W. R., "Some aspects of non-stationary airfoil theory and its practical application," *J. Aeronautical Sciences*, Vol. 8, No. 3, 1941, pp. 379–390.
- ¹⁸Amiet, R. K., "Compressibility effects in unsteady thin-airfoil theory," *AIAA J.*, Vol. 12, No. 2, 1974, pp. 252–255.
- ¹⁹Cunha, G. and Redonnet, S., "On the signal degradation induced by the interpolation and the sampling rate reduction in aeroacoustics hybrid methods," *Int. J. Num. Methods Fluids*, Vol. 71, No. 7, March 2013, pp. 910929.
- ²⁰Schnell, R., Yin, J., Funke, S., and Siller, H., "Aerodynamic and Basic Acoustic Optimization of a Contra- Rotating Open Rotor with Experimental Verification," *18th AIAA/CEAS Aeroacoustics Conference*, No. AIAA paper 2012-2127, Colorado Springs, CO, USA, 2012.